Astronomy & Astrophysics manuscript no. output
July 21, 2026
©ESO 2026

Superorbital variability in the quiescent black hole X-ray transient A0620–00

Enzo A. Saavedra[1,2], Roi Alonso[1,2], Teo Muñoz-Darias[1,2], Jorge Casares[1,2], Manuel A. P. Torres[1,2], Montserrat Armas Padilla[1,2], James F. Steiner[3], David M. Russell[4], Gastón J. Escobar[1,2], Federico García[5,6], Fraser Lewis[7,8], Daniel Mata Sánchez[1,2], and Pablo Rodríguez-Gil[1,2]

[1] Instituto de Astrofísica de Canarias (IAC), Vía Láctea s/n, La Laguna 38205, S/C de Tenerife, Spain
[2] Departamento de Astrofísica, Universidad de La Laguna, La Laguna, E-38206, S/C de Tenerife, Spain
[3] Center for Astrophysics | Harvard & Smithsonian, 60 Garden St, Cambridge, MA 02138, USA
[4] Center for Astrophysics and Space Science (CASS), New York University Abu Dhabi, UAE
[5] Instituto Argentino de Radioastronomía (CCT La Plata, CONICET; CICPBA; UNLP), C.C.5, (1894) Villa Elisa, Argentina
[6] Facultad de Ciencias Astronómicas y Geofísicas, Universidad Nacional de La Plata, B1900FWA La Plata, Argentina
[7] Faulkes Telescope Project, Cardiff, Wales, UK
[8] The Schools' Observatory, Astrophysics Research Institute, Liverpool John Moores University, 146 Brownlow Hill, Liverpool L3 5RF, UK

Received; accepted

ABSTRACT

Quiescent black hole low-mass X-ray binaries provide a key setting for probing accretion physics at low luminosities. A0620–00, the archetypal system in this class, has remained in X-ray quiescence for decades and exhibits complex optical variability, yet the long-term behaviour of its accretion flow remains poorly understood. Here, we report an analysis of long-term optical monitoring of A0620–00 from ZTF, LCO, and ATLAS. The full dataset spans nearly two decades, with the ZTF light curve providing the primary $\sim$ 2760-day baseline for the period analysis. We identify a superorbital cycle with a period of $P = 261.9 \pm 9.4$ d and a peak-to-peak amplitude of $\sim$ 0.2 mag. The signal is recovered independently across all three surveys, and red-noise simulations indicate that it is unlikely to arise from stochastic variability alone. Furthermore, the relative occurrence of the *passive* and *active* quiescent states displayed by the system seems to depend on the superorbital phase, with passive states concentrated near the cycle minimum and active states more common near maximum. We find that, among the possible interpretations, retrograde nodal precession of a hot inner accretion flow might be able to explain the observed long-term modulation. In this interpretation, the periodic signal may arise from cyclic reorientation of the inner flow, which modulates the photometric contribution from the innermost regions. The inferred modulation period would correspond to a characteristic dynamical radius of $\sim 0.13a$ ($\sim 10^4\ R_g$), where a is the binary semi-major axis, broadly consistent with the expected transition between the outer thin disc and the inner hot accretion flow.

Key words. accretion, accretion disks — X-rays: binaries — stars: black holes — stars: individual: A0620–00

1. Introduction

A0620–00 (hereafter A0620) is a well-studied transient black hole low-mass X-ray binary (BH-LMXB) located at a distance of 1.06 ± 0.12 kpc (Cantrell et al. 2010), making it one of the closest known stellar-mass black holes. Since its discovery in outburst in 1975 (Elvis et al. 1975), A0620 has remained in X-ray quiescence, enabling detailed dynamical characterisation. The binary comprises a K-type companion star of 0.4 $M_\odot$ orbiting a $\sim$6 $M_\odot$ BH (McClintock & Remillard 1986; Cantrell et al. 2010; van Grunsven et al. 2017), with an orbital period of 7.75 hours and an orbital decay rate of $\dot{P} \approx -0.60$ ms yr^{-1} (González Hernández et al. 2014).

The optical light curve of A0620 observed during its long-term X-ray quiescence is far from steady, exhibiting complex variability that has been classified into distinct states (Cantrell et al. 2008, 2010). The *passive* state is dominated by the ellipsoidal modulation of the donor star, which is produced by the different projected area of the Roche lobe-shaped donor across the orbit (e.g., van Grunsven et al. 2017). This modulation traces the system's baseline luminosity. By contrast, A0620 frequently enters an *active* state characterised by aperiodic flaring, an increased mean flux, and significant colour variability.

The sources of optical emission in quiescent BH systems are not fully understood. Current evidence suggests that an advection-dominated accretion flow (ADAF; Narayan & Yi 1994; Yuan & Narayan 2014) governs the inner disc regions at sufficiently low accretion rates (e.g., McClintock & Remillard 2000; Froning et al. 2011). This picture is expected to be particularly relevant when BHs are in quiescence ($L < 10^{-6} L_{\rm Edd}$). In the outer regions, the disc is thought to follow the standard geometrically thin, optically thick solution (Shakura & Sunyaev 1973), and its radiation can be approximated by a multicolour blackbody. Thus, the optical emission of A0620 in quiescence includes the companion star together with additional non-stellar components associated with the accretion flow. Donor-subtracted observations further reveal an optical/UV component and a red/infrared excess in quiescence; these may arise in the outer disc or stream–disc impact region, and possibly also from a weak compact jet, circumbinary material, or thermal bremsstrahlung from a warm outflow (e.g., Froning et al. 2007, 2011; Muno & Mauerhan 2006; Gallo et al. 2007;

Cherepashchuk et al. 2019; Zuo et al. 2025). A jet contribution is further supported by the radio and mm detections, as well as by strong near-IR variability and low-level polarization in the reddest bands (Gallo et al. 2006; Russell et al. 2016; Dinçer et al. 2018; Gallo et al. 2019; dePolo et al. 2022). Variability in these components may contribute to the observed transitions between the different optical quiescent states.

This complex long-term optical behaviour motivates the question of whether part of the variability of A0620 in quiescence may be organised on timescales much longer than the orbital period. A possible superorbital modulation of ∼255 d has previously been reported in A0620 from long-term optical monitoring, although with only marginal significance (Leibowitz et al. 1998). Superorbital flux modulations are well documented in X-rays in high-mass X-ray binaries and in the optical in cataclysmic variables, predominantly in systems accreting at comparatively high rates. Across these systems, the proposed mechanisms for superorbital modulations include disc precession, radiation-driven warping, and variations in the mass-transfer rate (Kotze & Charles 2010, 2012; Fragile et al. 2026). In LMXBs, convincing cases are rarer, and the clearest examples are found in neutron star systems. These include ultracompact X-ray binaries (i.e. with $P_{\rm orb} \lesssim 80$ min; e.g., Armas Padilla et al. 2023), such as 4U 1820–303 and 47 Tuc X–9 (Richman et al. 1994; Tudor et al. 2018), as well as other neutron star LMXBs such as 4U 1636–53 (Shih et al. 2005). However, such cases remain rare, and in BH-LMXBs these modulations have generally been reported in bright sources (see e.g., Kotze & Charles 2012). This difficulty is not only a matter of the typically longer orbital periods of BH-LMXBs, but also of the fact that they spend most of their lifetimes in quiescence.

In an attempt to address this gap, we use optical monitoring from different facilities to search for long-term modulations in A0620. We describe the observational data set in the following section; in Section 3 we analyse and evaluate the significance of a 262 d periodicity identified in these data, and in Section 4 we discuss possible origins of this signal.

2. Photometric data

Long-term optical photometry of A0620 was retrieved from the Zwicky Transient Facility (ZTF), the Las Cumbres Observatory (LCO) and the Asteroid Terrestrial-impact Last Alert System (ATLAS). A summary of these observations, including the temporal coverage and number of data points for each facility, is presented in Table 1. The ZTF dataset, spanning ∼2800 d, provides the primary baseline for our period analysis.

2.1. Zwicky Transient Facility

A0620 was observed using the ZTF, a time-domain survey based on the Palomar 48-inch Schmidt Telescope (Masci et al. 2019). ZTF features a 600-megapixel camera with a 47 deg^2 field of view, surveying the northern visible sky at ∼ 3760 deg^2 h^{-1} and achieving median depths of $g \approx 20.8$ and $r \approx 20.6$ (AB; 5σ in 30 s). The A0620 dataset released in DR24 spans = 58204–60968, comprising 348 and 334 epochs in the r- and g-bands, respectively. The ZTF pipeline provided photometric and astrometric calibration with relative photometric accuracy $\lesssim 2\%$ versus Pan-STARRS DR1. Simultaneous data from four comparison stars within the same field were included (see Fig. 1 and Table 2). The ZTF monitoring covers a total baseline of ∼ 2764 d, structured into seven seasonal observing windows with an average duration of ∼ 206 d.

Table 1: Log of Photometric Observations.

Telescope	Filter	- 2400000 Range	Span (d)	$N_{\rm obs}$
ZTF	g	58204–60968	2764	334
ZTF	r	58216–60968	2752	348
LCO	V	53750–60740	6988	523
LCO	i	53750–60740	6989	651
ATLAS	o	57318–60540	3222	2420
ATLAS	c	57313–60400	3087	690

Notes. The - 2400000 range is rounded to the nearest integer.

2.2. Las Cumbres Observatory

A0620 has been regularly monitored in the optical during the last ∼ 20 yr with the LCO 2 m and 1 m robotic telescopes, from 2006 January 15 ($\rm HJD_{TDB}$ = 2453750) to 2025 March 3 ($\rm HJD_{TDB}$ = 2460740), mostly using V and i filters. The images have been processed and analysed by the recently developed XBNEWS pipeline, which downloads the reduced images (i.e., bias, dark, and flat-field corrected images) from the LCO archive, automatically rejects poor-quality reduced images, performs astrometry using *Gaia* DR2 positions and carries out multi-aperture photometry (MAP; Stetson 1990), solves for photometric zero-point offsets between epochs (Bramich & Freudling 2012), and flux-calibrates the photometry using the ATLAS-REFCAT2 catalogue (Tonry et al. 2018). If the target is not detected in an image above the detection threshold, then XBNEWS performs forced MAP at the target coordinates. In this case, we reject all forced MAP magnitudes with an uncertainty > 0.25 mag, as these are very uncertain photometric measurements. For further details on XBNEWS, see Russell et al. (2019) and Goodwin et al. (2020). For further details of the LCO/Faulkes monitoring of A0620, see Zuo et al. (2025). Up to this analysis cutoff date, a total of 651 and 523 reliable magnitudes in the i and V bands, respectively, were obtained during our ongoing long-term optical monitoring of A0620 with LCO.

2.3. Asteroid Terrestrial-impact Last Alert System

A0620 was also observed with ATLAS (Tonry et al. 2018), which consists of four 0.5 m telescopes located in Hawaii, Chile, and South Africa. ATLAS surveys a large fraction of the sky with approximately a daily cadence. ATLAS' telescopes employ customised filters *cyan* (c; covering 420–650 nm) and *orange* (o; covering 560–820 nm). Forced photometry[1] of A0620 was conducted from = 57313–60540 using photometry measured on the ATLAS reduced images. Flux calibration relied on the ATLAS Refcat2 catalogue.

3. Analysis and results

We first characterised the long-term optical variability of A0620 across the available datasets. For each survey and filter we computed the mean magnitudes and root-mean-square (rms) dispersions, obtaining $r = 17.5 \pm 0.1$ mag and $g = 18.6 \pm 0.1$ mag from ZTF, $o = 17.4 \pm 0.2$ mag and $c = 18.1 \pm 0.2$ mag from ATLAS, and $V = 17.6 \pm 0.3$ mag and $i = 17.1 \pm 0.1$ mag from LCO.

To assess whether the variability is intrinsic to A0620 rather than an instrumental artefact, we selected comparison stars from

[1] https://fallingstar-data.com/forcedphot/

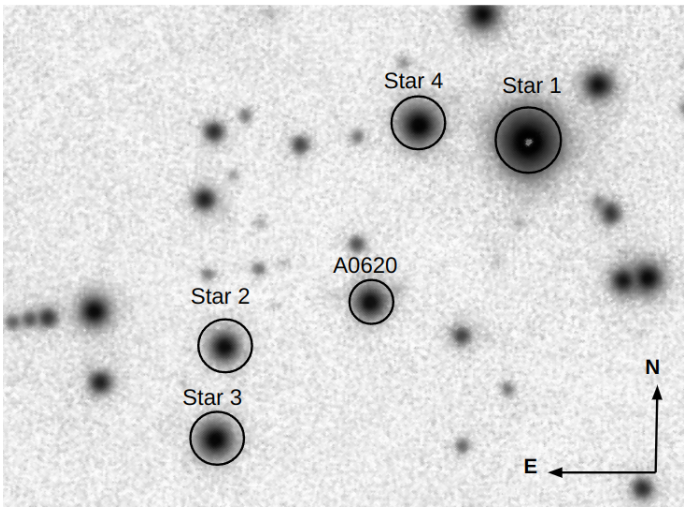


Fig. 1: Pan-STARRS DR1 (i, r, g) image showing A0620 and the comparison stars used in the ZTF data. The field of view is $\sim 1' \times 1'$.

the ZTF dataset with high-quality photometry (Fig. 1; Table 2). The comparison stars show low rms scatter, with $\sigma_g = 0.024$–0.066 mag and $\sigma_r = 0.026$–0.053 mag (Table 2). The rms dispersion in the A0620 photometry is ~ 2.5 times larger than the scatter observed in a comparison star with similar brightness, supporting the conclusion that the excess scatter is intrinsic to A0620.

As a first step, we performed a photometric classification following Cantrell et al. (2010) into passive and active states (see Fig. 2). We implemented this separation by modelling the lower envelope of the phase-folded light curve, using the orbital period and reference epoch (7.75234 h and $\mathrm{HJD_{TDB}} = 2446082.6671$; González Hernández et al. 2014). Specifically, we fitted a second-order Fourier series in orbital phase to the faint end of the magnitude distribution (defined by the 75th percentile in phase bins) to establish the stable passive baseline; this model is overplotted in the phased light curve for reference. We then computed the residuals of the full dataset relative to this model. Data consistent with the baseline (residuals $\lesssim 0.1$ mag, allowing for photometric noise) were classified as passive, while those exhibiting significant excess brightness were classified as active (see Fig. 2). During these active intervals, the system brightens by $\Delta m \approx 0.3$ mag relative to the passive state across different orbital phases (e.g., from $r \approx 17.4$ to 17.1 at phase 0.25, and from 17.5 to 17.2 at phase 0.5), implying that the excess emission accounts for at least $\sim 25\%$–30% of the total optical flux. This classification approach yields a physically motivated distinction between intervals governed by the ellipsoidal modulation of the donor star (i.e., passive state) and those dominated by aperiodic variability (i.e., active state).

3.1. Long-term periodicity

In light of the observed variability, we computed single-band Lomb–Scargle (LS) periodograms independently for each filter on the full A0620 light curve, that is, including both the passive and active states, see Fig. 3 (Lomb 1976; Scargle 1982). We restricted the LCO and ATLAS observations to epochs after $\mathrm{HJD_{TDB}} = 2458212$, to maximise cross-survey overlap and avoid calibration changes at earlier epochs (see below). Each dataset showed that the highest-power peak corresponds to a period of

Table 2: Mean ZTF magnitudes of A0620 and comparison stars.

Star	g mag	σ_g (mag)	r mag	σ_r (mag)
1	15.25	0.024	14.63	0.026
2	18.56	0.066	17.63	0.053
3	17.87	0.049	17.07	0.033
4	17.63	0.048	16.69	0.037
A0620	18.59	0.166	17.47	0.134

Notes. Mean g- and r-band magnitudes and light-curve rms dispersions are given for A0620 and the four comparison stars in the ZTF dataset. The σ columns list the light-curve rms dispersion.

$\sim$262 d, with additional peaks at $\sim$155 d (likely the first harmonic) and $\sim$643 d (likely a sub-harmonic of the main signal). These periodicities were confirmed by additional analysis using phase dispersion minimisation (Stellingwerf 1978) and the non-uniform fast Fourier transform method (Garrison et al. 2024). The distributions of the LS period estimates are adequately described by a Gaussian; we therefore combine the band-by-band period estimates through an inverse-variance weighted mean, using their 1σ statistical uncertainties to define the weights (Table 3). Propagating these statistical errors into the combined, band-averaged period yields $P = 261.9 \pm 8_{\mathrm{stat}}$ d.

To account for band-to-band differences and for reasonable variations in time span and state selection, we further include a systematic contribution to the period uncertainty, estimated from the scatter between the periods obtained in the different filters and from these alternative analyses, which contributes $\sigma_{P,\mathrm{sys}} = 5$ d and is added in quadrature to the statistical term[2]. Our final constraint on the long-term modulation is therefore $P = 261.9 \pm 8_{\mathrm{stat}} \pm 5_{\mathrm{sys}} = 261.9 \pm 9.4$ d (234–290 d with 3σ confidence). The peak-to-peak variations are consistent with ~ 0.2 mag across all cases. Semi-amplitudes show no significant dependence on passband; for instance, the g-band semi-amplitude is 0.10 ± 0.01, comparable to 0.085 ± 0.009 in the r band.

To define a common superorbital ephemeris, we fitted each band independently with a sinusoid of fixed period $P = 261.9$ d, leaving the mean level, amplitude, and phase free. We define T_0 as the epoch of maximum magnitude of the modulation, corresponding to the faint phase of the cycle. The fitted T_0 values cluster around $\mathrm{HJD_{TDB}} = 2459520$, although modest band-to-band offsets remain. Because the single-sinusoid fits show excess scatter relative to the formal photometric uncertainties, we rescaled the phase uncertainties to account for the intrinsic variability before combining the measurements. The resulting representative common epoch is $T_0[\mathrm{HJD_{TDB}}] = 2459520 \pm 6$. This value is adopted as the common reference epoch throughout this work.

3.2. On the Significance of the Periodicity

To quantify the confidence in this periodicity, we assessed its statistical significance by calculating the false alarm probability (FAP) for each peak and converting it to σ significance with the inverse standard normal survival function using the `astropy` li-

[2] We define the systematic uncertainty as the sample standard deviation of the set of periods $\{P_i\}$ obtained from the different bands and alternative analyses, $\sigma_{P,\mathrm{sys}} = \left[\sum_{i=1}^{N}(P_i - \bar{P})^2/(N-1)\right]^{1/2}$, where $\bar{P}$ is their mean and N is the number of measurements. The total uncertainty is then $\sigma_{P,\mathrm{tot}} = (\sigma^2_{P,\mathrm{stat}} + \sigma^2_{P,\mathrm{sys}})^{1/2}$.

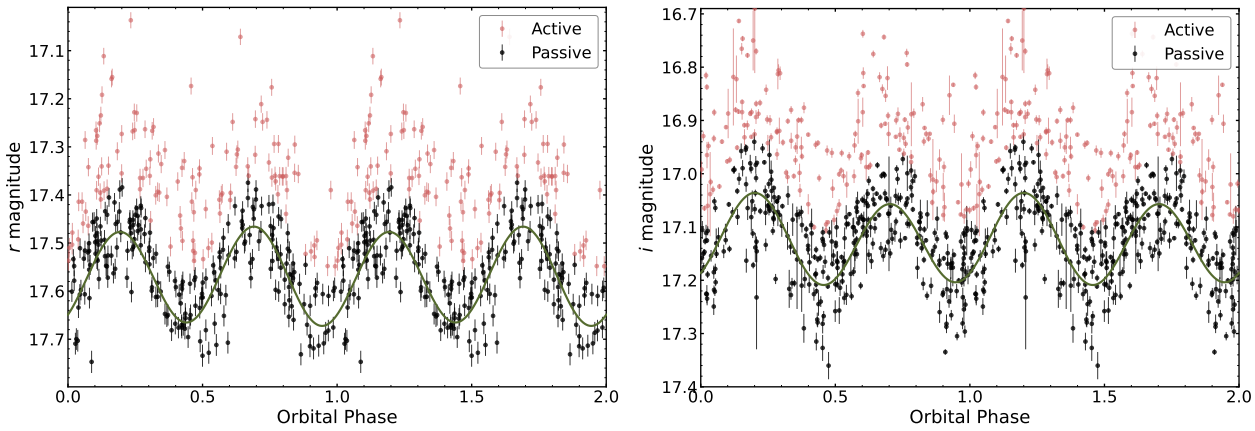


Fig. 2: ZTF-r (left) and LCO-i (right) light curves of A0620, folded at the orbital period. The plots illustrate the ellipsoidal modulation, distinguishing between active (red) and passive (black) states. The green curve shows the Fourier model used to define the passive baseline.

brary (Astropy Collaboration et al. 2022). The ∼ 262-day peak reaches equivalent single-trial Gaussian significances of 6.6σ in the r band and 5.8σ in the g band. The ATLAS o and c bands give significances of 10σ and 4.6σ, respectively. While the LCO data also indicate the presence of the 262 d periodicity, it remains below the 3σ threshold; this is plausibly due to the smaller effective baseline/cadence and larger photometric error in the LCO sample relative to ZTF/ATLAS.

We tested whether the 262-day peak could arise from red noise. We fitted the log–log power-spectrum continuum (masking the 262 d peak and its harmonics), obtaining power-law slopes $\alpha_r = 0.35 \pm 0.07$ and $\alpha_g = 0.32 \pm 0.15$ for the r and g bands, respectively. Using these slopes, we simulated 2×10^5 red-noise light curves with the actual sampling and photometric errors (see e.g., Timmer & König 1995; Saavedra et al. 2025), computed LS periodograms, and recorded the maximum power over 10–1000 d. In r, the power at $P = 262$ d lies in the extreme tail of the simulated distribution, corresponding to a global significance of $\simeq 5\sigma$ (and $\simeq 4.8\sigma$ in g). Given the finite number of simulations, we refrain from quoting a more precise value, but the result shows that the ∼ 262 d modulation is highly unlikely to be produced by red noise alone.

To assess potential contamination from residual differential photometry effects, we computed the periodogram of airmass as a function of observing time. This periodogram shows pronounced peaks at annual and semi-annual periods, consistent with seasonal visibility variations, whereas the periodogram of A0620 does not exhibit these features. The absence of these peaks suggests that chromatic effects do not dominate the observed periodicity, reinforcing the conclusion that the ∼ 262 d signal is intrinsic to A0620. To verify that ellipsoidal modulation did not contribute to the 262-day periodicity, we sampled the ellipsoidal model at the same observation epochs and computed its LS periodogram. No significant periodicity emerged. This indicates that the 262-day signal does not result from the continuous but partial sampling of the underlying ellipsoidal modulation. Having established this, we subtracted the best-fit ellipsoidal model from the observed light curves. The 262-day signal persists in the residuals with consistent amplitude, and hereafter all analyses are performed on these ellipsoidal-subtracted light curves unless stated otherwise.

To investigate intermittent signals and the evolution of the ∼262-day modulation, we computed moving Lomb-Scargle (LS) periodograms (Kalicinsky et al. 2020; VanderPlas 2018). We monitored general source behaviour by mapping signal power and amplitude within a 1000-day sliding window. The results of this detectability analysis show that in early LCO epochs ($\mathrm{HJD_{TDB}} \lesssim 2458750$), where sampling is sparse ($N \simeq 70$–175), the LS power remains below the threshold (see Fig. 4). We attribute this non-detection to the combination of poor phase coverage and stochastic noise contamination, which effectively raises the noise floor. However, as cadence improves after $\mathrm{HJD_{TDB}} \sim 2458750$ ($N \gtrsim 210$), the modulation becomes significantly detected. The ZTF r-band data, with consistently denser sampling ($N \simeq 250$), exceeds the threshold in all windows, supporting that the signal is persistent but requires sufficient cadence to emerge from the stochastic noise in the active states.

To explore whether these early non-detections might be primarily a sampling artifact, we performed a Monte Carlo rejection test. We selected the most densely sampled 1800-day window in the LCO dataset ($N = 322$) and randomly downsampled it to match the observation count of our sparsest early window ($N = 64$). Across 10^4 iterations, we found that in ≈15.4% of the trials, this artificial degradation produced an LS power equal to or weaker than the actual value observed during the early epochs. This result indicates that the apparent absence of the modulation before $\mathrm{HJD_{TDB}} \sim 2458750$ is statistically compatible with sparse sampling.

Table 3: Periods obtained from each band periodogram.

	r	g	i	V	o	c
Period [d]	264.8	262.1	263.4	258.9	260.4	268.9
Error [d]	18.3	19.8	12.7	11.4	15.4	24.9

Notes. Periods and errors (1σ) are given in units of days. The periodograms are associated with each band for the epochs ranging from MJD 58212 to 59998.

3.3. Phase-Folded Light Curves

We folded the light curves using the superorbital ephemeris defined above, adopting $P = 261.9$ d and $T_0[\mathrm{HJD_{TDB}}] = 2459520$, and calculated median magnitudes in 0.1-phase bins. Fig. 3 (right panels) shows a similar modulation in A0620 across all

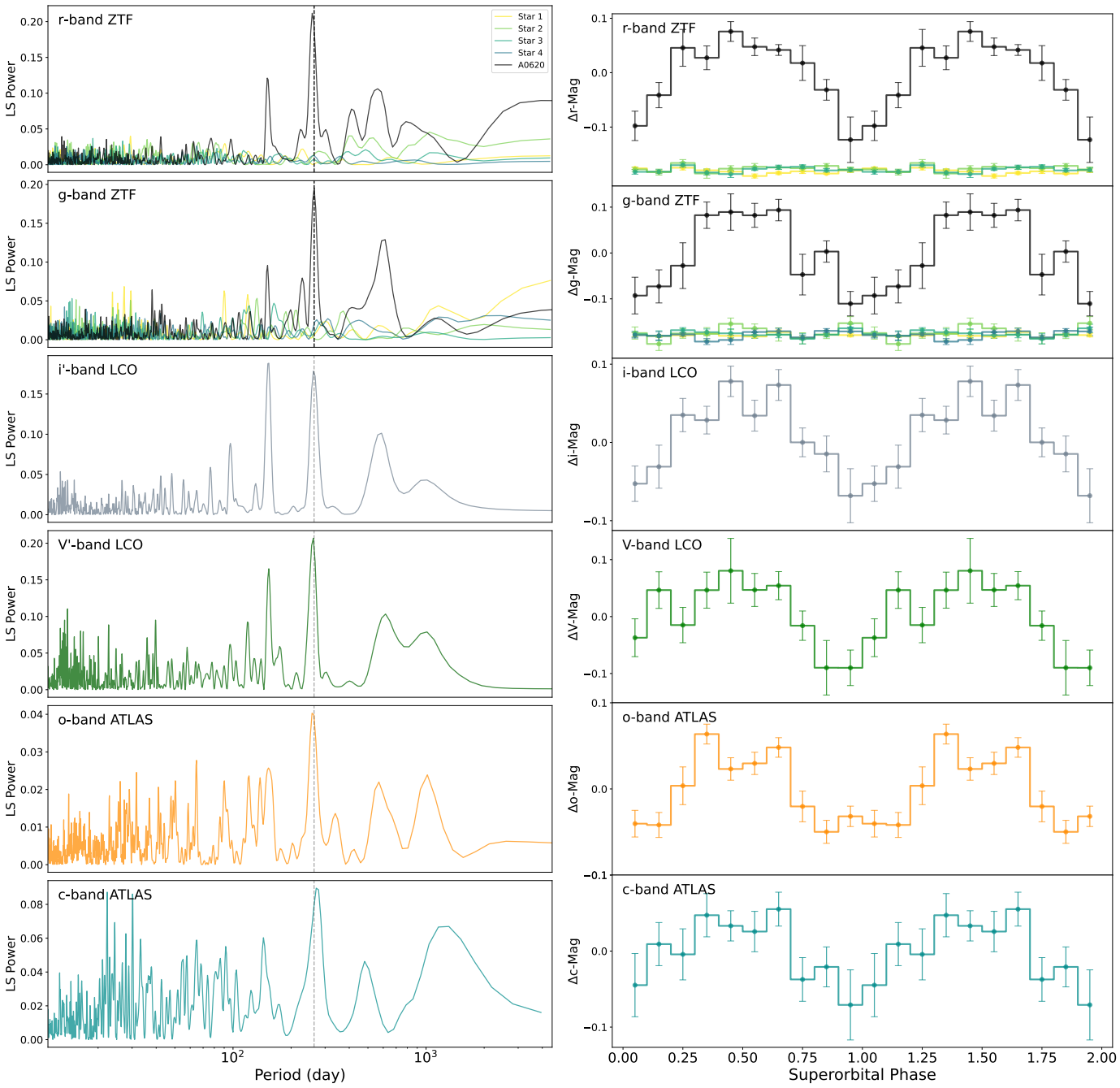


Fig. 3: Left: LS periodograms of A0620 from multi-survey photometry. The upper panels show ZTF *g*- and *r*-band power spectra (comparison stars included). The lower panels present LCO (*i*-, *V*-band) and ATLAS (*o*- and *c*-band) periodograms. The 262-d periodicity (vertical dashed line) appears consistently across all datasets. Right: Corresponding phase-folded light curves at P = 262 d. ZTF *g*- and *r*-band data (top panels) include comparison stars offset by 0.18 mag. ATLAS and LCO data (bottom four panels) show coherent modulation across all bands, supporting the periodicity.

bands when the data are phase-folded on this ephemeris. In contrast, the comparison stars remain statistically constant under identical analysis, supporting that the periodic variability is intrinsic to A0620.

In an effort to better visualise the long-term periodicity, the ZTF *r*-band and LCO *i*-band were binned into 26 d intervals. The median was computed for each bin and a sinusoidal model with a period of 262 days was plotted (see Fig. 5). Although significant residuals are evident, the 262-day modulation broadly traces the long-term evolution of the system flux, with the maxima roughly corresponding to epochs dominated by the active state and the minima to passive periods.

To further understand the connection between the 262-day variability and the quiescent-state classification, we computed histograms of the passive and active data points in ten equal superorbital phase ($\phi_{\rm sup}$) bins and obtained their phase-dependent fractions (see Fig. 6). In the ZTF-*r* data, the $\phi_{\rm sup}$ = 0.0–0.1 bin contains 29 passive and 3 active points, corresponding to passive and active fractions of 91% and 9%, respectively. By contrast, the $\phi_{\rm sup}$ = 0.5–0.6 bin contains 13 passive and 19 active points,

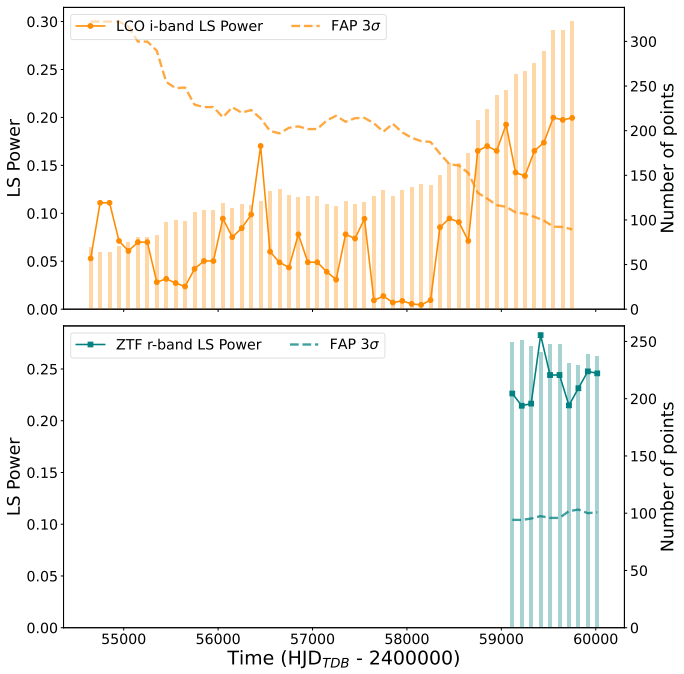


Fig. 4: Periodogram analysis as a function of time. LS power at 262 d (filled circles), the 3σ false-alarm threshold (dashed lines) and the number of observations per segment (shaded bars).

corresponding to 41% and 59%, respectively. Around $\phi_{\rm sup} \simeq 0.5$, the passive fraction therefore drops substantially, while the active fraction increases. A similar behaviour is seen in the LCO-*i* data. The $\phi_{\rm sup} = 0.0$–0.1 bin contains 35 passive and 19 active points, corresponding to passive and active fractions of 65% and 35%, respectively. In the $\phi_{\rm sup} = 0.5$–0.6 bin, these numbers change to 21 and 40, corresponding to 34% and 66%. Around $\phi_{\rm sup} \simeq 0.5$, the passive fraction therefore drops while the active fraction increases, a behaviour seen across both datasets.

4. Discussion

In this work, we report evidence for superorbital variability in A0620. We detect a superorbital modulation at 261.9 ± 9.4 d ($> 5\sigma$) with a peak-to-peak amplitude of ~ 0.2 mag. The feature is recovered independently in the ZTF, ATLAS, and LCO datasets, making instrumental or survey-specific systematics improbable. Since the comparison stars show no analogous behaviour, these results suggest that the periodicity is likely intrinsic to A0620.

A more detailed inspection shows that the $\sim$ 262-day modulation is most clearly recovered in the ZTF dataset over the interval $\simeq$ 58700–60000, corresponding to roughly five cycles. The same feature is also seen in the ATLAS data over a similar time span. In the longer-baseline LCO data, however, the periodicity is recovered less uniformly; as shown by the moving periodograms (see Fig. 4), it is more prominent during some epochs and less evident during others. In particular, the signal is weaker prior to HJD$_{\rm TDB} \sim 2458700$.

It remains unclear whether this reduced visibility arises from changes in the intrinsic behaviour of the source, sparse sampling in the earlier part of the LCO light curve, additional stochastic noise, or some combination of these effects. Although we cannot rule out genuine long-term intermittency, the behaviour seen during the better-sampled intervals, together with the overall consistency across datasets, suggests that sparse sampling may be the dominant explanation for the apparent weakening of the feature in the early LCO data. Even so, the overall behaviour remains consistent with the $\sim$255 d cycle reported by Leibowitz et al. (1998), despite the marginal significance of that earlier detection. The fact that two independent analyses, separated by nearly three decades, recover similar periods lends further support to the presence of a long-term cycle in A0620.

The phase histograms show that the relative fractions of the two quiescent-state classifications vary with superorbital phase, with passive points more frequent near $\phi_{\rm sup} \simeq 0$ and active points near $\phi_{\rm sup} \simeq 0.5$. This indicates that the $\sim$262-day modulation is linked not only to the long-term flux evolution, but also to the changing relative occurrence of the two quiescent states. By definition, during intervals classified as active, individual data points frequently lie well outside the sinusoidal trend, with deviations of up to $\sim$0.2 mag (Fig. 2). This is comparable to the peak-to-peak amplitude of the long-term cycle itself (see Fig. 5). This behaviour is consistent with the superposed aperiodic variability that characterises the active state (Cantrell et al. 2008, 2010), which has been attributed to the inner accretion flow and/or the jet (Shahbaz et al. 2004; Veledina et al. 2013; Gallo et al. 2006, 2019; Russell et al. 2016). We now consider the physical mechanisms that could account for both the long-term modulation and its connection to the state-dependent optical variability in A0620.

4.1. Nodal Precession of the Hot Inner Flow

A plausible scenario is the retrograde *nodal precession* of the accretion flow, driven by the tidal torque of the companion star on a misaligned disc structure. In this scenario, the angular-momentum vector of the tilted flow precesses retrogradely around the binary angular-momentum vector due to the companion's gravitational pull. This is a dynamical effect analogous to the nodal precession of the Moon's orbit, which is tilted with respect to the Earth's orbital plane and precesses under the influence of the Sun's gravity. This gradual change in disc orientation produces a periodic modulation in the observed emission that can naturally reach timescales of hundreds of days. Disc precession of this kind has been proposed to explain the long-term evolution observed in several X-ray binaries, including the persistent neutron-star system Her X-1, with its well-known ≈ 35 d cycle (Katz 1973; Gerend & Boynton 1976; Wijers & Pringle 1999).

To assess whether this interpretation is dynamically plausible, we apply the formalism for a fluid disc subject to binary torques (Papaloizou & Terquem 1995; Larwood et al. 1996; Bate et al. 2000). Assuming the precessing structure behaves as a rigid body, the relationship between the precession period $P_{\rm prec}$ and the orbital period $P_{\rm orb}$ is described by:

$$\left|\frac{P_{\rm orb}}{P_{\rm prec}}\right| = \frac{15}{32}\frac{q}{\sqrt{1+q}}\left(\frac{R_{\rm d}}{a}\right)^{3/2}\cos\delta, \tag{1}$$

where $q = M_2/M_1$ is the mass ratio, a is the binary separation, and δ is the tilt angle (assumed small, $\cos\delta \approx 1$). Substituting the system parameters for A0620 ($P_{\rm orb} \approx 0.323$ d, $P_{\rm prec} \approx 261.9$ d, $q \approx 0.06$) into Eq. 1, we infer the characteristic radius ($R_{\rm d}$) that would reproduce this precession frequency:

$$\frac{R_{\rm d}}{a} = \left[\frac{32}{15}\frac{\sqrt{1+q}}{q}\left(\frac{P_{\rm orb}}{P_{\rm prec}}\right)\right]^{2/3} \approx 0.13. \tag{2}$$

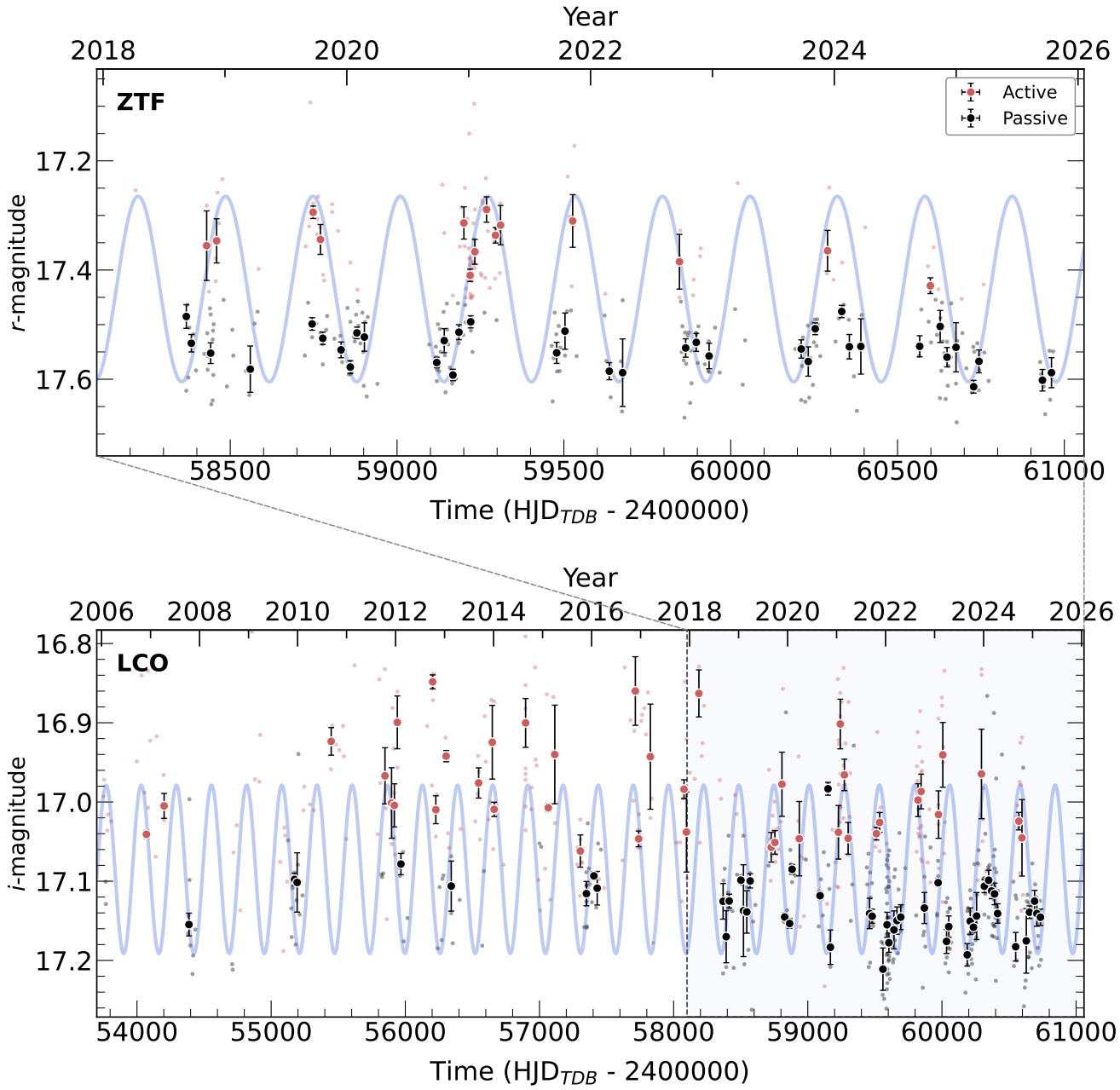


Fig. 5: Light curves of A0620 covering the long-term modulation. *Top:* ZTF *r*-band. *Bottom:* LCO *i*-band.
The panels cover different timescales, with lines indicating the zoom-in from the ZTF baseline to the LCO period. In both panels, the faint background points show the individual observations, while the larger points show the median in 26-day bins, with error bars derived from the median absolute deviation. A sinusoidal model with a period of 262 days is overplotted in each panel, and all points are colour-coded according to the source state.

This derived radius ($R_{\rm d} \approx 0.13\,a \approx 3.6 \times 10^4 R_{\rm g}$) locates the precessing structure deep within the disc, well inside the expected outer disc edge ($R_{\rm out} \sim 0.7\,R_{\rm L1}$, where $R_{\rm L1}$ denotes the effective Roche lobe radius of the compact object; Frank et al. 2002). A possible solution involves a transition radius between the outer cold, thin disc and the hot inner flow in quiescent BH-LMXBs ($\sim 10^4\ R_{\rm g}$; see e.g., Narayan et al. 1996; Esin et al. 1997; McClintock & Remillard 2000; Froning et al. 2011; Yuan & Narayan 2014, see Fig. 7 for a schematic representation).

In quiescence, the accretion flow is likely stratified into two distinct regions: an outer geometrically thin disc and an inner hot, moderately thick flow (e.g., Narayan et al. 1996; Esin et al. 1997). If a misalignment is present, the ability of the flow to precess coherently depends on how efficiently this tilt, or warp, is communicated between neighbouring radii. This can proceed in two limiting regimes: through bending waves when $\alpha \lesssim H/R$, or diffusively when $\alpha \gtrsim H/R$, where H is the local vertical scale height of the accretion flow and R is the cylindrical radius measured in the plane of the disc (Papaloizou & Pringle 1983; Papaloizou & Lin 1995; Lubow et al. 2002). In the outer thin disc, where H/R is small ($H/R \ll 1$; Shakura & Sunyaev 1973), the diffusive regime is likely to dominate, at least for commonly adopted quiescent-disc viscosities (e.g. Dubus et al. 2001; Meyer-Hofmeister & Meyer 2001). This would make it

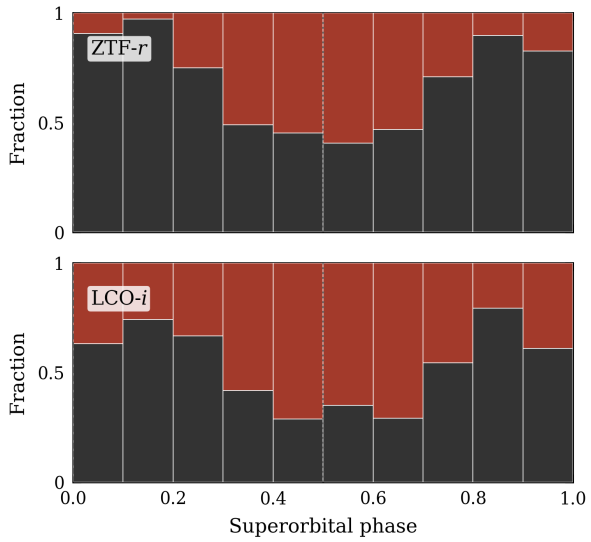


Fig. 6: Phase histograms of the passive and active classifications. Black denotes the passive fraction and red denotes the active fraction. The histograms are normalised by the total number of observations in each of ten equal superorbital phase bins. The upper and lower panels correspond to the ZTF-r and LCO-i data, respectively.

more difficult to sustain a coherent global response to tidal perturbations over large radii. We note that in the aforementioned case of Her X-1 the situation is significantly different because it is a persistent system characterised by an irradiated, optically thick, geometrically thin disc. In such luminous, irradiated discs, warps can be maintained by external torques, such as radiative and stream-impact torques. The companion tidal torque can then drive coherent precession over larger radii (e.g., Wijers & Pringle 1999; Kosec et al. 2022).

As discussed above, for the case of A0620 the precession radius derived for the quiescent superorbital modulation is consistent with the expected transition radius between the outer thin disc and the hot inner flow. For the precession scenario to produce observable photometric modulation, the inner accretion structure should retain a disc-like morphology while remaining thick enough to support coherent bending-wave communication, which requires $\alpha \lesssim H/R$. At the inferred precession radius, the radial sound-crossing time is expected to be much shorter than the precession period, allowing such a compact inner accretion structure to remain radially coupled and precess approximately as a coherent body (Larwood et al. 1996; Larwood 1998). We therefore refer to this component as a hot inner flow, a structure with ADAF-like thermodynamic properties but with a moderately thick, disc-like geometry with H/R in the range of $\sim 0.1 - 0.5$ (e.g., Ingram et al. 2009; Das & Sharma 2013; Yuan & Narayan 2014; Marcel et al. 2018; see Fig. 7). Thus, if the observed precession originates within the accretion flow, the hot inner flow is the more plausible precessing component.

This interpretation also offers a plausible explanation for the observed phase-dependent occurrence of the two quiescent states, with precession remaining active and cyclically modulating the geometric visibility of the hot inner flow. When the orientation of the hot inner flow reduces its projected contribution, the optical emission would be dominated by the donor star and its ellipsoidal modulation, corresponding to the passive state. Conversely, when the hot flow becomes more directly visible, it would contribute a larger fraction of the total optical flux, producing active-state behaviour. If this geometric picture is correct, it should leave distinctive imprints on the wavelength dependence and viewing-angle sensitivity of the modulation.

The weak chromatic dependence of the modulation offers an additional constraint. The semi-amplitudes in the g and r bands are 0.10 ± 0.01 and 0.085 ± 0.009 mag, respectively, implying a nearly achromatic signal ($A_g/A_r \approx 1.18$). Such behaviour is broadly consistent with a geometric origin, in which the variability is driven primarily by changes in viewing angle or path length. By contrast, intrinsic accretion-rate fluctuations would generally be expected to produce stronger variability at bluer wavelengths, while synchrotron emission from a jet might enhance the modulation at longer wavelengths (Russell et al. 2006; Gallo et al. 2006). The present data do not exclude these alternatives completely, however. For example, frequency-dependent optical depths within the flow could still introduce mild chromatic effects (Mahadevan 1997; Veledina et al. 2013). Thus, although the measured amplitudes are compatible with the geometric interpretation, broader wavelength coverage extending into the near-infrared or ultraviolet will be required to distinguish conclusively between these possibilities.

A further geometric diagnostic is provided by the system's viewing angle, which governs the amplitude of any projection-driven modulation. The inclination of A0620 ($i \approx 50°$; Cantrell et al. 2010; van Grunsven et al. 2017) is well suited for detecting geometric modulation from a precessing inner structure. A tilted disc-like surface that contributes a fraction f of the total optical flux produces a peak-to-peak fractional variation that scales as $\Delta F/F_{\rm total} \approx 2\, f\, \delta\, \tan i$[3], where δ is the tilt angle. At this inclination, $\tan i \approx 1.2$, providing appreciable geometric sensitivity while remaining below the regime where self-shadowing or grazing-angle effects would dominate. Since the donor star dominates the optical flux in the passive state, the hot inner flow likely contributes of order one-third of the total optical flux near active-state maximum. Taking this dilution into account, a tilt angle of $\delta \approx 15°$ is sufficient to account for the observed ~ 0.2 mag modulation. The same geometric picture naturally predicts that the modulation amplitude should depend on the system viewing angle: in higher-inclination systems ($i \gtrsim 70°$), the steeper projection effects could produce stronger variability or even periodic obscuration episodes, whereas in nearly face-on configurations ($i \lesssim 20°$) the signal would be largely washed out.

The geometric scenario also carries implications beyond the optical band. Because the X-ray emission in quiescence also originates in the hot inner flow, a corresponding superorbital modulation in X-rays would be expected if the optical signal is indeed geometric in nature. However, the quiescent X-ray luminosity of A0620 is extremely low ($L_X \sim 10^{30.8}$ erg s^{-1}; McClintock et al. 1995), placing such a detection well beyond the reach of current instrumentation. Future X-ray missions with improved soft-band sensitivity could provide an independent test of the precession scenario.

Beyond A0620 itself, the geometric interpretation proposed here is consistent with the growing observational evidence for spin-orbit misalignment in BH-LMXBs. Variations in the jet axis observed during outbursts in V404 Cyg (Miller-Jones et al. 2019) and MAXI J1820+070 (Poutanen et al. 2022) suggest that

[3]For a flat emitting surface, the projected area scales as $\cos i$. A tilt δ causes the effective viewing angle to oscillate between $i \pm \delta$. The peak-to-peak change in projected area is $\cos(i-\delta) - \cos(i+\delta) = 2 \sin i \, \sin\delta \approx 2\delta \sin i$ for small δ. Normalising by the unperturbed area ($\cos i$) gives a fractional variation of $2\delta \tan i$.

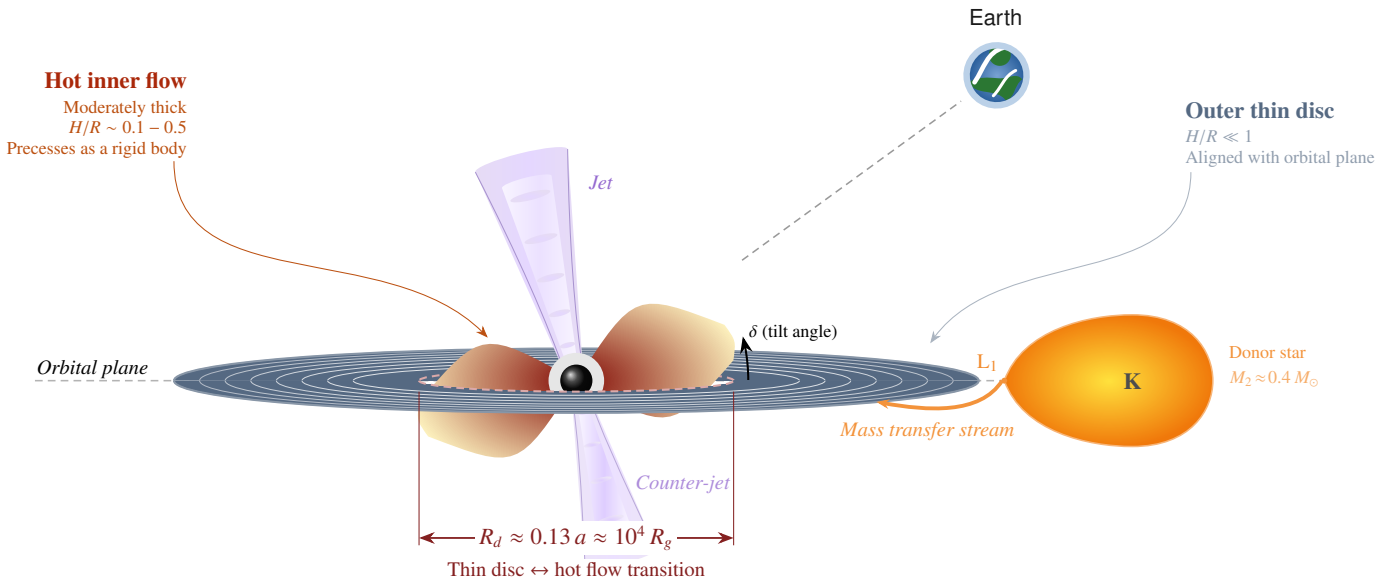


Fig. 7: Schematic view of the geometry considered for A0620–00 in the nodal-precession scenario discussed in this work (not to scale). The outer thin disc (blue) is aligned with the orbital plane. The hot inner flow (orange-red gradient) is moderately thick ($H/R \sim 0.1 - 0.5$), misaligned by an angle δ, and precesses as a rigid body. Collimated relativistic jets emerge perpendicular to the hot inner flow midplane. The donor star is shown filling its Roche lobe. The observer is shown at an inclination of $\sim 50°$ relative to the orbital axis (van Grunsven et al. 2017).

tilted inner structures are present in this population (see Fragile et al. 2026, for a review). The detection of a superorbital modulation in A0620 during deep quiescence suggests that precessing inner flows may remain dynamically active even at luminosities far below outburst. However, this geometric interpretation remains to be tested with dedicated simulations to determine whether a misaligned hot inner flow in A0620 can sustain tidal precession and reproduce the observed superorbital modulation.

4.2. Alternative scenarios

Several other mechanisms can also produce long-term optical variability. We examine four possibilities for A0620, including apsidal precession, a hierarchical triple configuration, viscous diffusion, and magnetic activity of the donor star. Although each is physically motivated, none provides a clear explanation for the observed modulation without additional assumptions or independent supporting evidence.

Apsidal precession can occur in LMXBs when tidal torques from the donor star excite resonant modes in the accretion disc, particularly in systems with mass ratios $q = M_2/M_1 \lesssim 0.33$ (Whitehurst & King 1991). With $q \approx 0.06$ (Neilsen et al. 2008), A0620 satisfies this low-q condition in principle. Using the formalism of Patterson et al. (2003), the fractional superhump excess can be expressed as

$$\Delta P^{-1} = [(P_{\rm sh} - P_{\rm orb})/P_{\rm orb}]^{-1} = \left[0.37\,q/(1+q)^{1/2}\right]^{-1} \eta^{-2.3} - 1, \tag{3}$$

where $P_{\rm sh}$ is the superhump period and $\eta \approx 0.8$ parameterises the radial extent of the disc (Mineshige et al. 1992). The corresponding apsidal precession period is $P_{\rm prec} = (1/P_{\rm orb} - 1/P_{\rm sh})^{-1}$. Substituting the parameters of A0620 yields $P_{\rm prec} \approx 25$ d, more than an order of magnitude shorter than the observed 262-day modulation. Therefore, although apsidal precession may operate in low-q systems, the standard resonant-disc framework does not reproduce the timescale observed in A0620.

A *hierarchical triple system* is another possibility, especially given the discovery of a tertiary companion in the BH-LMXB V404 Cyg (Burdge et al. 2024). In this scenario, a third body could perturb the inner binary and drive secular eccentricity oscillations through the Kozai–Lidov mechanism (Kozai 1962; Lidov 1962). This mechanism has also been invoked to explain superorbital modulations in other X-ray binaries such as 4U 1820–303 and 47 Tuc X–9 (Chou & Grindlay 2001; Tudor et al. 2018). The characteristic Kozai–Lidov timescale is

$$T_{\rm KL} \simeq \frac{16}{30\pi}\frac{P_3^2}{P_{\rm orb}}\frac{M_{\rm tot}}{M_3}(1-e_3^2)^{3/2}, \tag{4}$$

where $M_{\rm tot} = M_1 + M_2 + M_3$, and P_3 and e_3 are the orbital period and eccentricity of the tertiary companion (Naoz 2016). For the quiescent magnitude and distance of A0620 (Cantrell et al. 2008, 2010), a companion contributing only $\sim 10\%$ of the optical flux would have $M_V \gtrsim 10$, consistent with a late-type main-sequence star such as an M2.5V companion ($M_3 \sim 0.4\ M_\odot$; Pecaut & Mamajek 2013). For this fiducial tertiary mass, reproducing the observed $\sim$ 262 d modulation requires $P_3 \approx 5.2 - 6.4$ d for $0 \le e_3 \le 0.5$; these configurations satisfy the standard hierarchical stability criteria (Mardling & Aarseth 2001). Using Kepler's third law, this corresponds to an outer separation of $a_{\rm out} \approx 0.11 - 0.13$ AU. Given the inner binary separation $a_{\rm in} = 0.0176$ AU (González Hernández et al. 2014), this implies a very compact configuration with $a_{\rm out}/a_{\rm in} \approx 6 - 7$. Thus, although a hierarchical triple configuration cannot be ruled out, there is currently no independent evidence for a tertiary companion in A0620. Moreover, while the Kozai–Lidov mechanism can produce cyclic changes in the inner binary geometry, it would not by itself explain the observed association between the periodic signal, the passive/active states, and changes in the accretion-related variability. These considerations make this scenario less compelling.

Viscous diffusion through the outer disc can also produce timescales comparable to the observed superorbital period. Using the standard α-disc scaling (Shakura & Sunyaev 1973; Frank

et al. 2002), $t_{\rm visc} \approx 3.5 \times 10^5 \alpha^{-4/5} R_{10}^{5/4} m_1^{1/4} \dot{M}_{16}^{-3/10}$ s, where $R_{10} = R_{\rm out}/10^{10}$ cm, $\dot{M}_{16} = \dot{M}/10^{16}$ g s^{-1}, and m_1 is the BH mass in solar units. For the parameters of A0620 (Marsh et al. 1994; Cantrell et al. 2010; Froning et al. 2011), a 262 d viscous timescale would imply $\alpha \approx 0.02$. This value is consistent with theoretical expectation for quiescent accretion discs, where low ionization levels reduce turbulent activity (e.g. Menou et al. 2000; Dubus et al. 2001). However, the process is not uniform across the disc due to the radial dependence of the timescale, $t_{\rm visc} \propto R^{5/4}$. The outer regions act as a low-pass filter, damping high-frequency fluctuations from the donor while preserving variations on the order of the viscous timescale. While this mechanism can explain the characteristic duration of the phase-dependent state occurrence, it does not naturally produce a periodic signal like the one observed at $\sim$ 262 days. Therefore, this hypothesis appears to be unfavourable.

Finally, a *magnetic activity cycle* of the K-type donor star could also modulate the mass-transfer rate. The K-type donor star in A0620 is expected to be tidally locked to the binary orbit, giving a rotation period $P_{\rm rot} = P_{\rm orb} = 0.323$ d. In chromospherically active stars, magnetic cycles scale with the stellar rotation period through a ratio that depends on the Rossby number, with values spanning $P_{\rm cyc}/P_{\rm rot} \sim$ 100–1000 (Brandenburg et al. 2017; Strugarek et al. 2017; Kolláth & Oláh 2009; Saar & Brandenburg 1999). For A0620, the observed ratio $P_{\rm sup}/P_{\rm rot} = 262/0.323 \approx 810$ is consistent within this range. A plausible pathway by which such a cycle could imprint itself on the light curve is through modulation of the mass transfer rate. Cyclic changes in the coverage and distribution of starspots on the donor surface would alter the local effective temperature near the inner Lagrange point, shifting the effective Roche-lobe filling factor and thereby driving quasi-periodic variations in $\dot{M}$ (King et al. 2007). In addition, variations in magnetic pressure at the stellar surface could modulate the geometry of the mass transfer stream itself.

However, the empirical activity–rotation relations have been calibrated primarily on slowly rotating, partly convective solar-type stars, and their extrapolation to the rapidly rotating, fully or nearly convective donor in A0620 is uncertain. It is also unclear whether a magnetic cycle in such a star would produce a sufficiently coherent and large-amplitude signal to account for the $\sim$0.2 mag modulation observed here, given that the resulting $\dot{M}$ variations would still need to propagate through the disc before affecting the optical flux. This mechanism cannot be excluded with the present data, and could be tested through long-term spectroscopic monitoring of chromospheric activity indicators such as Hα (González Hernández & Casares 2010), which would track the donor's magnetic state independently of the accretion flow.

5. Conclusion

Using optical photometry spanning nearly two decades, we analysed the quiescent black-hole X-ray binary A0620–00. The data reveal a statistically robust superorbital modulation at $P = 261.9 \pm 9.4$ d that is unlikely to arise solely from instrumental effects or sampling artefacts. The observed periodicity is plausibly interpreted as the signature of retrograde nodal precession of the inner accretion flow. The corresponding dynamical radius of $\sim 0.13a$ places the precessing structure well within the outer disc edge, consistent with the expected transition radius between the outer thin disc and the hot inner accretion flow.

These results have direct implications for how accretion dynamics are interpreted in quiescent BH-LMXBs. If the observed modulation is indeed driven by nodal precession, then the inner accretion flow is not a static structure, but one with persistent behaviour whose cyclic geometric reorientation regulates the visibility of the inner region in the optical flux. This offers a plausible explanation for the phase-dependent occurrence of the active and passive states without necessarily invoking large changes in the mass transfer rate. The broader implications are also significant. If similar superorbital signals are present but remain undetected in other systems, then precessing inner flows may represent a fundamental, yet so far overlooked, feature of low-luminosity accretion.

High-cadence optical monitoring with next-generation facilities such as the Vera C. Rubin Observatory (and its LSST) will provide an important opportunity to determine whether similar superorbital signals are common among quiescent BH-LMXBs. At the same time, dedicated numerical simulations will be needed to test whether a misaligned hot inner flow can sustain coherent tidal precession and generate a long-period modulation comparable to that observed in A0620.

Acknowledgements. We thank the anonymous referee for their comments, which have improved the manuscript. We acknowledge support by Spanish Agencia Estatal de Investigación via PID2021-124879NB-I00, PID2022-143331NB-100 and PID2024-161863NB-I00. D.M.S. and M.A.P. acknowledge support through the Ramón y Cajal grants RYC2023-044941 and RYC2022-035388-I, funded by MCIU/AEI/10.13039/501100011033 and FSE+. DMR is supported by Tamkeen under the NYU Abu Dhabi Research Institute grant CASS. Funded by the European Union (Project 101183150 – OCEANS). Views and opinions expressed are, however, those of the author(s) only and do not necessarily reflect those of the European Union or the European Research Executive Agency (REA). Neither the European Union nor REA can be held responsible for them. This work makes use of observations from the Las Cumbres Observatory global telescope network. Based on observations obtained with the Samuel Oschin Telescope 48-inch and the 60-inch Telescope at the Palomar Observatory as part of the Zwicky Transient Facility project. ZTF is supported by the National Science Foundation under Grants No. AST-1440341 and AST-2034437 and a collaboration including current partners Caltech, IPAC, the Oskar Klein Center at Stockholm University, the University of Maryland, University of California, Berkeley, the University of Wisconsin at Milwaukee, University of Warwick, Ruhr University, Cornell University, Northwestern University and Drexel University. Operations are conducted by COO, IPAC, and UW.

References

Armas Padilla, M., Corral-Santana, J. M., Borghese, A., et al. 2023, A&A, 677, A186
Astropy Collaboration, Price-Whelan, A. M., Lim, P. L., et al. 2022, ApJ, 935, 167
Bate, M. R., Bonnell, I. A., Clarke, C. J., et al. 2000, MNRAS, 317, 773
Bramich, D. M. & Freudling, W. 2012, MNRAS, 424, 1584
Brandenburg, A., Mathur, S., & Metcalfe, T. S. 2017, ApJ, 845, 79
Burdge, K. B., El-Badry, K., Kara, E., et al. 2024, Nature, 635, 316
Cantrell, A. G., Bailyn, C. D., McClintock, J. E., & Orosz, J. A. 2008, ApJ, 673, L159
Cantrell, A. G., Bailyn, C. D., Orosz, J. A., et al. 2010, ApJ, 710, 1127
Cherepashchuk, A. M., Katysheva, N. A., Khruzina, T. S., et al. 2019, MNRAS, 483, 1067
Chou, Y. & Grindlay, J. E. 2001, ApJ, 563, 934
Das, U. & Sharma, P. 2013, MNRAS, 435, 2431
dePolo, D. L., Plotkin, R. M., Miller-Jones, J. C. A., et al. 2022, MNRAS, 516, 4640
Dinçer, T., Bailyn, C. D., Miller-Jones, J. C. A., Buxton, M., & MacDonald, R. K. D. 2018, ApJ, 852, 4
Dubus, G., Hameury, J.-M., & Lasota, J.-P. 2001, A&A, 373, 251
Elvis, M., Page, C. G., Pounds, K. A., Ricketts, M. J., & Turner, M. J. L. 1975, Nature, 257, 656
Esin, A. A., McClintock, J. E., & Narayan, R. 1997, ApJ, 489, 865
Fragile, P. C., Ingram, A., Musoke, G., & Ogilvie, G. I. 2026, arXiv e-prints, arXiv:2603.02993, accepted in Space Science Reviews
Frank, J., King, A., & Raine, D. J. 2002, Accretion Power in Astrophysics: Third Edition
Froning, C. S., Cantrell, A. G., Maccarone, T. J., et al. 2011, ApJ, 743, 26
Froning, C. S., Robinson, E. L., & Bitner, M. A. 2007, ApJ, 663, 1215

Gallo, E., Fender, R. P., Miller-Jones, J. C. A., et al. 2006, MNRAS, 370, 1351
Gallo, E., Migliari, S., Markoff, S., et al. 2007, ApJ, 670, 600
Gallo, E., Teague, R., Plotkin, R. M., et al. 2019, MNRAS, 488, 191
Garrison, L. H., Foreman-Mackey, D., Shih, Y.-h., & Barnett, A. 2024, Research Notes of the American Astronomical Society [arXiv:2409.08090], submitted for publication
Gerend, D. & Boynton, P. E. 1976, ApJ, 209, 562
González Hernández, J. I. & Casares, J. 2010, A&A, 516, A58
González Hernández, J. I., Rebolo, R., & Casares, J. 2014, MNRAS, 438, L21
Goodwin, A. J., Russell, D. M., Galloway, D. K., et al. 2020, MNRAS, 498, 3429
Ingram, A., Done, C., & Fragile, P. C. 2009, MNRAS, 397, L101
Kalicinsky, C., Reisch, R., Knieling, P., & Koppmann, R. 2020, Atmospheric Measurement Techniques, 13, 467
Katz, J. I. 1973, Nature Physical Science, 246, 87
King, A. R., Pringle, J. E., & Livio, M. 2007, MNRAS, 376, 1740
Kolláth, Z. & Oláh, K. 2009, A&A, 501, 695
Kosec, P., Kara, E., Fabian, A. C., et al. 2022, ApJ, 936, 185
Kotze, M. M. & Charles, P. A. 2010, MNRAS, 402, L16
Kotze, M. M. & Charles, P. A. 2012, MNRAS, 420, 1575
Kozai, Y. 1962, AJ, 67, 591
Larwood, J. 1998, MNRAS, 299, L32
Larwood, J. D., Nelson, R. P., Papaloizou, J. C. B., & Terquem, C. 1996, MNRAS, 282, 597
Leibowitz, E. M., Hemar, S., & Orio, M. 1998, MNRAS, 300, 463
Lidov, M. L. 1962, Planet. Space Sci., 9, 719
Lomb, N. R. 1976, Ap&SS, 39, 447
Lubow, S. H., Ogilvie, G. I., & Pringle, J. E. 2002, MNRAS, 337, 706
Mahadevan, R. 1997, ApJ, 477, 585
Marcel, G., Ferreira, J., Petrucci, P.-O., et al. 2018, A&A, 615, A57
Mardling, R. A. & Aarseth, S. J. 2001, MNRAS, 321, 398
Marsh, T. R., Robinson, E. L., & Wood, J. H. 1994, MNRAS, 266, 137
Masci, F. J., Laher, R. R., Rusholme, B., et al. 2019, PASP, 131, 018003
McClintock, J. E., Horne, K., & Remillard, R. A. 1995, ApJ, 442, 358
McClintock, J. E. & Remillard, R. A. 1986, ApJ, 308, 110
McClintock, J. E. & Remillard, R. A. 2000, ApJ, 531, 956
Menou, K., Hameury, J.-M., Lasota, J.-P., & Narayan, R. 2000, MNRAS, 314, 498
Meyer-Hofmeister, E. & Meyer, F. 2001, A&A, 372, 508
Miller-Jones, J. C. A., Tetarenko, A. J., Sivakoff, G. R., et al. 2019, Nature, 569, 374
Mineshige, S., Hirose, M., & Osaki, Y. 1992, PASJ, 44, L15
Muno, M. P. & Mauerhan, J. 2006, ApJ, 648, L135
Naoz, S. 2016, ARA&A, 54, 441
Narayan, R., McClintock, J. E., & Yi, I. 1996, ApJ, 457, 821
Narayan, R. & Yi, I. 1994, ApJ, 428, L13
Neilsen, J., Steeghs, D., & Vrtilek, S. D. 2008, MNRAS, 384, 849
Papaloizou, J. C. B. & Lin, D. N. C. 1995, ApJ, 438, 841
Papaloizou, J. C. B. & Pringle, J. E. 1983, MNRAS, 202, 1181
Papaloizou, J. C. B. & Terquem, C. 1995, MNRAS, 274, 987
Patterson, J., Thorstensen, J. R., Kemp, J., et al. 2003, PASP, 115, 1308
Pecaut, M. J. & Mamajek, E. E. 2013, ApJS, 208, 9
Poutanen, J., Veledina, A., Berdyugin, A. V., et al. 2022, Science, 375, 874
Richman, H. R., Applegate, J. H., & Patterson, J. 1994, PASP, 106, 1075
Russell, D. M., Bramich, D. M., Lewis, F., et al. 2019, Astronomische Nachrichten, 340, 278
Russell, D. M., Fender, R. P., Hynes, R. I., et al. 2006, MNRAS, 371, 1334
Russell, D. M., Shahbaz, T., Lewis, F., & Gallo, E. 2016, MNRAS, 463, 2680
Saar, S. H. & Brandenburg, A. 1999, ApJ, 524, 295
Saavedra, E. A., Muñoz-Darias, T., Torres, M. A. P., et al. 2025, A&A, 702, A103
Scargle, J. D. 1982, ApJ, 263, 835
Shahbaz, T., Hynes, R. I., Charles, P. A., et al. 2004, MNRAS, 354, 31
Shakura, N. I. & Sunyaev, R. A. 1973, A&A, 24, 337
Shih, I. C., Bird, A. J., Charles, P. A., Cornelisse, R., & Tiramani, D. 2005, MNRAS, 361, 602
Stellingwerf, R. F. 1978, ApJ, 224, 953
Stetson, P. B. 1990, PASP, 102, 932
Strugarek, A., Beaudoin, P., Charbonneau, P., Brun, A. S., & do Nascimento, J.-D. 2017, Science, 357, 185
Timmer, J. & König, M. 1995, A&A, 300, 707
Tonry, J. L., Denneau, L., Flewelling, H., et al. 2018, ApJ, 867, 105
Tudor, V., Miller-Jones, J. C. A., Knigge, C., et al. 2018, MNRAS, 476, 1889
van Grunsven, T. F. J., Jonker, P. G., Verbunt, F. W. M., & Robinson, E. L. 2017, MNRAS, 472, 1907
VanderPlas, J. T. 2018, ApJS, 236, 16
Veledina, A., Poutanen, J., & Vurm, I. 2013, Monthly Notices of the Royal Astronomical Society, 430, 3196–3212
Whitehurst, R. & King, A. 1991, MNRAS, 249, 25
Wijers, R. A. M. J. & Pringle, J. E. 1999, MNRAS, 308, 207
Yuan, F. & Narayan, R. 2014, ARA&A, 52, 529
Zuo, Z., Cugno, G., Michail, J., et al. 2025, ApJ, 991, 157